Kinematic and Dynamic Models of Hyper -Redundant Manipulator Based on Link Eigenvectors

Xiantong Xu, Haibo Xie, Cheng Wang, and Huayong Yang

***Abstract*—Hyper-redundant manipulator has a slim geometric shape and super high degrees of freedom (DOF), which promises high motion efficiency and flexible obstacle avoidance ability in a confined space. Nevertheless, it also challenges the more complicated motion control strategy. In this article, the concepts of "link eigenvectors" and "manipulator's eigenpoints," which apply to a widely used geometric kinematics method, are proposed. Hence, the kinematic and dynamic models can be constructed intuitively. And since the indirect joint space and local frames are replaced by the link eigenvectors and unified global frame, the kinematic and dynamic problems, especially the link's position, velocity, and acceleration, can be solved more directly. Further, based on the new models, mechanical analysis and Newton–Euler dynamic equations are effectively simplified, so as to realize the fast and precise dynamic resolution. Experiment results show that the kinematic and dynamic theoretical models are correct. And the driving forces of motors are successfully optimized, while the kinematic precision is improved simultaneously.**

***Index Terms*—Dynamic model, hyper-redundant manipulator, kinematic model, Newton–Euler method.**

I. Introduction

SINCE the mid-term of last century, robotics has been progressively promoted, and a growing number of occasions have realized the working mode of "robot replacing human," such as industrial automation, minimally invasive surgery [1], [2], in-space inspection [3], nuclear reactor maintenance and repairing [4], and search and rescue [5]. However, the traditional robot, which is limited by its degrees of freedom (DOF), profile, and size, is difficult to achieve a high-precision and dexterous obstacle avoidance motion in a narrow space. As a result, it is increasingly difficult to satisfy the practical application with the development in productivity. Thus, hyper-redundant manipulator [6] with shape similar to snake [7], or elephant trunk [8], [9], or octopus tentacle [10] has received much more attention over the past decades. And, their motion control technology has been developed unprecedentedly.

Traditional forward kinematics refers to solving the end effector pose in the reference frame by the known joint parameters. And inverse kinematics refers to solving the joint parameters by the given end effector pose. Since traditional robots have low DOFs, and their joint space, configuration space, and local coordinate systems are related closely, their forward and inverse kinematics can be resolved quickly by the algebraic or numerical method. Yet, due to the super high DOFs of hyper-redundant manipulator, the algebraic or numerical inverse kinematics is too complex.

Thus, the geometric method, which refers to the specific tracking geometric curve method, is particularly widely used, such as the methods of tracking the reference curves [11], [12], follow-the-leader [13], FABRIK [14], and segmented geometry [15]. These geometric methods normally generate the reference curves that the manipulator can track in the task space, and then force the manipulator to fit the curves. That optimizes the inverse resolution by reducing the computation cost. By fitting the reference curve, the method would get the positions of the link ends directly, and then the links' poses can be expressed by the link ends conveniently. Thus, in the scope of this method, the reference curve can be treated as the forward solution, while the links' poses can be treated as the inverse solution. That means the regular joint space and configuration space are substituted by the links' poses, and the local coordinate systems are not needed anymore.

As early as the 1970s, various inverse dynamics methods had already been studied [16], [17], [18]. Rodriguez [19] even figured out a way to solve the inverse and forward dynamic problems with $O(N)$ solutions. Since then, quantities of dynamic researches on cable-driven manipulators have been done to extend the early studies, such as Euler-Lagrange formalism [20], Cosserat rod theory [21], [22], Newton–Euler dynamics [23], [24], [25], and principle of virtual work [26], [27]. To improve the computation efficiency, Amouri et al. [28] proposed a dynamic model that disregards the friction effects, which

Manuscript received 4 April 2023; revised 13 June 2023; accepted 2 August 2023. Date of publication 28 August 2023; date of current version 18 April 2024. Recommended by Technical Editor Jens Kober and Senior Editor Jun Ueda. This work was supported in part by the Fundamental Research Funds for the Central Universities, Award Number 226-2022-00016, in part by State Key Laboratory of Fluid Power and Mechatronic Systems Independent Project, Award Number SKLoFP_ZZ_2106, in part by the National Key R&D Program of China, Award Number 2022YFC3802300. *(Corresponding author: Haibo Xie.)*

The authors are with the State Key Laboratory of Fluid Power & Mechatronic Systems, Zhejiang University, Hangzhou 310027, China (e-mail: ritonxu@zju.edu.cn; hbxie@zju.edu.cn; chwang@zju.edu.cn; yhy@zju.edu.cn).

Color versions of one or more figures in this article are available at https://doi.org/10.1109/TMECH.2023.3302853.

Digital Object Identifier 10.1109/TMECH.2023.3302853

might cause a bit of model error. Yuan et al. [29] presented a simpler way to analyze and verify the influence of cable friction. Although these studies successfully achieve dynamic analyses, they all still build dynamic models with joint parameters and local coordinate systems. That means the traditional methods haven't taken full use of the geometric method.

In order to solve all the global kinematic variables through the positions of the link ends directly and intuitively, the concepts of manipulator's eigenpoints and link eigenvectors are proposed in the kinematic field of the tracking geometric curve method. Then the kinematic and dynamic models are also reconstructed. As the new models are defined in a global coordinate system, some acceleration components that would be generated with the utilization of a rotating reference frame are avoided. Therefore, the Newton–Euler equations are simplified and the manipulator's dynamics are solved efficiently. The main contributions of this article are following.

1) The traditional local coordinate systems are abandoned and the simpler and more intuitive kinematic model of the manipulator is reconstructed.
2) Based on several assumptions, the mechanics of the cable-driven snake-like manipulator (CSM) is analyzed accurately and globally.
3) Based on the kinematic model and mechanical analysis, the dynamic model is constructed and the Newton–Euler method is simplified. The dynamics method is intuitive and can improve the static and dynamic performances of CSM.

The rest of the article is organized as follows. Section II is the kinematics part. It introduces the mechanical design of the CSM and the new kinematic model. Section III is the dynamics part. First, the forces on cables, links, etc., are analyzed in detail, and then the inverse dynamics are studied and demonstrated. Section IV is the experiment part. Both static and dynamic experiments show the effectiveness of the proposed method. Finally, Section V concludes this article.

II. Kinematics

A. Mechanical Design of CSM

The mechanical structure of CSM in the article is shown in Fig. 1. It has three parts, sliding table, base box, and arm span.

The sliding table provides the translation DOF for CSM.

The base box including the frame and the driving modules supplies the driving forces for the arm span's motion. The driving modules transmit the forces, i.e., transmitting the motor torques into the cable driving forces.

The arm span is composed of connecting the fixed link, six universal joints, five normal links, and the end link in series. And the fixed link is indexed as Link_0, the end link is Link_6. The normal links are indexed as $\text{Link}_1, \text{Link}_2, \ldots \text{Link}_5$. The distal end of the fixed link, both ends of the normal link, and the proximal end of the end link all have discs with holes for cables passing through. The discs' centers are indexed as $O_{a1}, O_{b1}, O_{a2}, O_{b2}, \ldots O_{a6}, O_{b6}$ from the fixed link to the end link. The joints are indexed as $\text{Joint}_1, \text{Joint}_2, \ldots \text{Joint}_6$, and Joint_0 is the fixed joint. Fig. 2(b) shows the view from the distal end of Link_i. And it sets the center of Joint_i as the origin, the axis

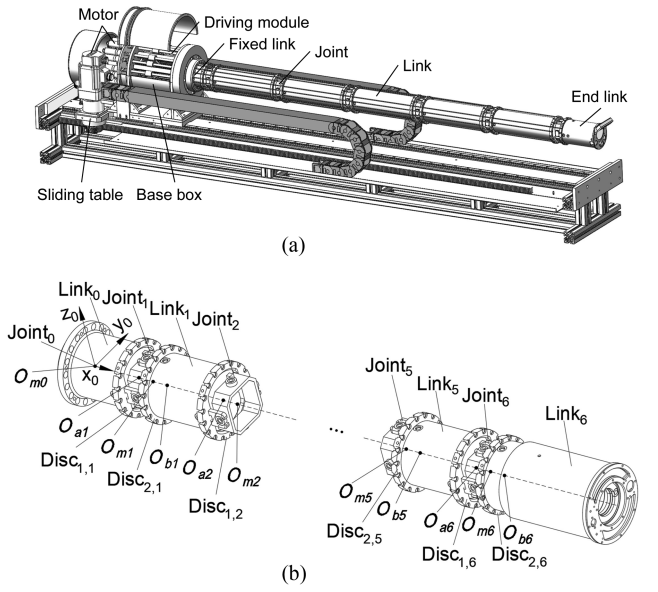

Fig. 1. Structure of CSM. (a) Mechanical structure of CSM. (b) Arm span.

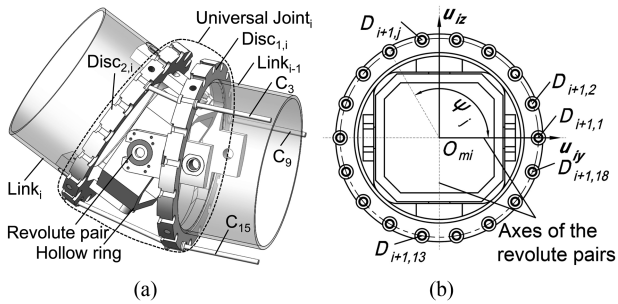

Fig. 2. Universal joint. (a) Structure of the joint. (b) Holes arrangement on $\text{Disc}_{1,i+1}$.

of the revolute pair between Link_i and Joint_{i+1} as $\boldsymbol{u_{iy}}$, whose direction is radial outward, the axis of the revolute pair between Link_i and Joint_i as $\boldsymbol{u_{iz}}$, whose direction is radial outward too, the central axis of Link_i as $\boldsymbol{u_{ix}}$, whose direction is from the proximal end to the distal end. The specific $\boldsymbol{u_{ix}}, \boldsymbol{u_{iy}}, \boldsymbol{u_{iz}}$ will be calculated in Section II–B. The holes on discs are evenly circumferentially distributed. The hole located on the proximal disc $\text{Disc}_{2,i}$ of Link_i and $\boldsymbol{u_{iy}}$ is indexed as $P_{i,1}$, and the rest holes are indexed counterclockwise as $P_{i,2}, P_{i,3}, \ldots P_{i,j} \ldots P_{i,18}$. Similarly, the hole located on the distal disc $\text{Disc}_{1,i+1}$ and $\boldsymbol{u_{iy}}$ is indexed as $D_{(i+1,1)}$, and the rest holes are indexed counterclockwise as $D_{i+(1,2)}, \ldots D_{(i+1,j)} \ldots D_{(i+1,18)}$. $\text{Disc}_{1,i}$ and $\text{Disc}_{2,i}$ belong to the same Joint_i. Ψ_j is the included angle between $\overrightarrow{O_{ai}D_{i,j}}$ and $\overrightarrow{O_{ai}D_{i,1}}$ and also the included angle between $\overrightarrow{O_{bi}P_{i,j}}$ and $\overrightarrow{O_{bi}P_{i,1}}$

$$\Psi_j = 2\,(j-1)\,\pi/\,(3\times 6)\,. \tag{1}$$

The cables passing through the corresponding holes are indexed as $\text{C}_1, \text{C}_2, \ldots \text{C}_j \ldots \text{C}_{18}$. As is shown in Fig. 2, each> universal joint with two DOFs is driven by three cables, i.e.,

Joint$_i$ is driven by C_i, C_{i+6}, C_{i+12}. The three cables would pass through the two discs of Link$_0$, Link$_1$, ... Link$_{i-1}$ and the proximal disc of Link$_i$. The base box can alter the lengths of C_i, C_{i+6}, C_{i+12} in Joint$_i$ by controlling the movement of C_i, C_{i+6}, C_{i+12}, so as to alter the distances between $D_{i,i}$ and $P_{i,i}$, $D_{i,i+6}$ and $P_{i,i+6}$, $D_{i,i+12}$ and $P_{i,i+12}$. And finally, Joint$_i$ rotates as required.

The structure puts the bulky power unit rear, making the arm span lighter and motion more flexible.

B. Construction of Kinematic Model

Definition: *Manipulator's eigenpoints* are the set of proximal and distal end points of all links.

Since there is no torsional motion between the adjacent links, the manipulator's eigenpoints can fully determine the position and attitude of the manipulator. Thus, it can be taken as the kinematic model. In traditional kinematics, the pose information of the manipulator is described with many local coordinate systems. These local coordinate systems can be transformed into each other with transformation matrices. However, the tracking geometric curve method gets the manipulator's eigenpoints first but not the joint parameters, so it is indirect and troublesome to solve the transformation matrices utilizing joint parameters. Therefore, although the traditional kinematic model is universal, it's not as simple and intuitive as the reconstructed kinematic model utilizing manipulator's eigenpoints directly. Additionally, the reconstructed dynamic model based on the new kinematic model can avoid the discussion of some acceleration components and is more efficient and intuitive.

Actually, manipulator's eigenpoints are enough to describe the motion state, but it is necessary to introduce the more important concept of link eigenvectors.

Definition: Link$_i$'s independent *link eigenvector* is a unit vector pointing from the proximal end to the distal end of Link$_i$. It is

$$\boldsymbol{u_{ix}} = \overrightarrow{O_{mi}O_{m(i+1)}} \Big/ \left|\overrightarrow{O_{mi}O_{m(i+1)}}\right| \tag{2}$$

$\boldsymbol{u_{ix}}$: Independent eigenvector.
O_{mi}: Proximal end of Link$_i$.

Link$_i$ also has two derived link eigenvectors, $\boldsymbol{u_{iy}}$and$\boldsymbol{u_{iz}}$, which is shown in Fig. 2(b).

Let $\boldsymbol{u_{dirz}} = \boldsymbol{u_{ix}} \times \boldsymbol{u_{(i-1)y}}$, then $\boldsymbol{u_{dirz}}$ is collinear with $\boldsymbol{u_{iz}}$.

Let $\boldsymbol{u_{diry}} = \boldsymbol{u_{dirz}} \times \boldsymbol{u_{ix}}$, then $\boldsymbol{u_{diry}}$ is collinear with $\boldsymbol{u_{iy}}$.

Therefore

$$\begin{cases} \boldsymbol{u_{iz}} = \boldsymbol{u_{dirz}} / \left|\boldsymbol{u_{dirz}}\right| \\ \boldsymbol{u_{iy}} = \boldsymbol{u_{diry}} / \left|\boldsymbol{u_{diry}}\right| \end{cases} \tag{3}$$

It can improve the accuracy of $\boldsymbol{u_{iy}}$ and$\boldsymbol{u_{iz}}$ by determining their directions first and then normalizing them respectively.

As is shown in Fig. 1(b), the global coordinate system can be defined as: The view is from the distal end of Link$_0$. Set the proximal end of Link$_0$ as the origin. Set $\overrightarrow{O_{m0}O_{m1}}$ as x$_0$-axis. Set y$_0$-axis horizontally to the right. Set z$_0$-axis vertically upward. Then, vectors $\boldsymbol{u_{0x}}, \boldsymbol{u_{0y}}, \boldsymbol{u_{0z}}$ is defined to coincide with the global coordinate system. If the manipulator's eigenpoints are known, $\boldsymbol{u_{ix}}(i = 1, 2 \cdots 6)$ can be calculated by (2), $\boldsymbol{u_{iy}}, \boldsymbol{u_{iz}}(i = 1, 2 \cdots 6)$ can be calculated by (3). Thus, all link eigenvectors can be calculated. Conversely, manipulator's eigenpoints can be calculated by the recursive formula,

$$O_{mi} = l_{(i-1)}\ \boldsymbol{u_{(i-1)x}} + O_{m(i-1)}\ (i = 12 \cdots 7) \tag{4}$$

$l_{(i-1)}$: Length of Link$_{(i-1)}$, i.e., $l_{(i-1)} = \left|\overrightarrow{O_{m(i-1)}O_{mi}}\right|$.

It is worth noting that the link eigenvectors are highly collinear with the link's inertial principal axes.

Actually, link eigenvectors and O_{mi} can be transformed into transformation matrix. Let ${}^0_i\boldsymbol{T}$ refers to the transformation matrix from the global coordinate system to the local coordinate system fixed on Link$_i$, then,

$${}^0_i\boldsymbol{T} = \begin{bmatrix} \boldsymbol{u_{ix}} & \boldsymbol{u_{iy}} & \boldsymbol{u_{iz}} & O_{mi} \\ 0 & 0 & 0 & 1 \end{bmatrix}. \tag{5}$$

As is shown in Fig. 2(a), there is a hollow ring numbered i (HR$_i$) in the universal joint. Analogously, HR$_i$ also has its own eigenvectors, $\boldsymbol{v_{ix}}, \boldsymbol{v_{iy}}, \boldsymbol{v_{iz}}$. Due to HR$_i$'s symmetrical structure, its eigenvectors are collinear with the inertial principal axes and their values are

$$\begin{cases} \boldsymbol{v_{iy}} = \boldsymbol{u_{(i-1)y}} \\ \boldsymbol{v_{iz}} = \boldsymbol{u_{iz}} \\ \boldsymbol{v_{ix}} = \boldsymbol{v_{iy}} \times \boldsymbol{v_{iz}} \end{cases}. \tag{6}$$

C. Mapping From Link Eigenvectors to Cables' Lengths

The cable C$_j$ within the range of arm span can be divided into the part between $P_{i-1,j}$ and $D_{i,j}$, and the part between $D_{i,j}$ and $P_{i,j}$, i.e., the link's part and the joint's part. After the cable is tensioned, the length of the link's part is fixed, while the length of the joint's part, i.e., the cable's length of C$_j$ between the two discs in Joint$_i$, is approximately equal to the distance between $D_{i,j}$ and $P_{i,j}$. Therefore, the following will only consider the joint's part. The symbols are defined as follows:

d : Distance from joint's center to one adjacent disc's center, i.e., $d = |O_{mi} - O_{ai}| = |O_{mi} - O_{bi}|$.
r_d : Radius of the distribution circle of the hole on the disc.
$s_{i,j}$: Distance between $D_{i,j}$ and $P_{i,j}$.
C_{sj}: Pseudo total length of C$_j$, calculated by the adding of related $s_{i,j}$.

Then (O_{ai} and O_{bi} have been defined in Section II–A),

$$\begin{cases} O_{ai} = O_{mi} - d\boldsymbol{u_{(i-1)x}} \\ O_{bi} = O_{mi} + d\boldsymbol{u_{ix}} \end{cases} (i = 1, 2, \cdots 6). \tag{7}$$

Let the initial values of $O_{b0}$and $P_{0,j}$be $O_{b0}(0, 0, 0)$ and $P_{0,j}(0, r_d\cos(\Psi_j), r_d\sin(\Psi_j))$ $(j = 1, 2 \cdots 18)$, then,

$$\begin{cases} D_{i,j} = P_{i-1,j} + O_{ai} - O_{b(i-1)} \\ P_{i,j} = r_d\ \cos(\Psi_j)\,\boldsymbol{u_{iy}} \\ \quad + r_d \sin(\Psi_j)\,\boldsymbol{u_{iz}} + O_{bi} \end{cases} (i = 1 \cdots 6). \tag{8}$$

Thus,

$$s_{i,j} = |P_{i,j} - D_{i,j}|\,(i = 1, 2, \cdots 6, j = 1, 2 \cdots 18). \tag{9}$$

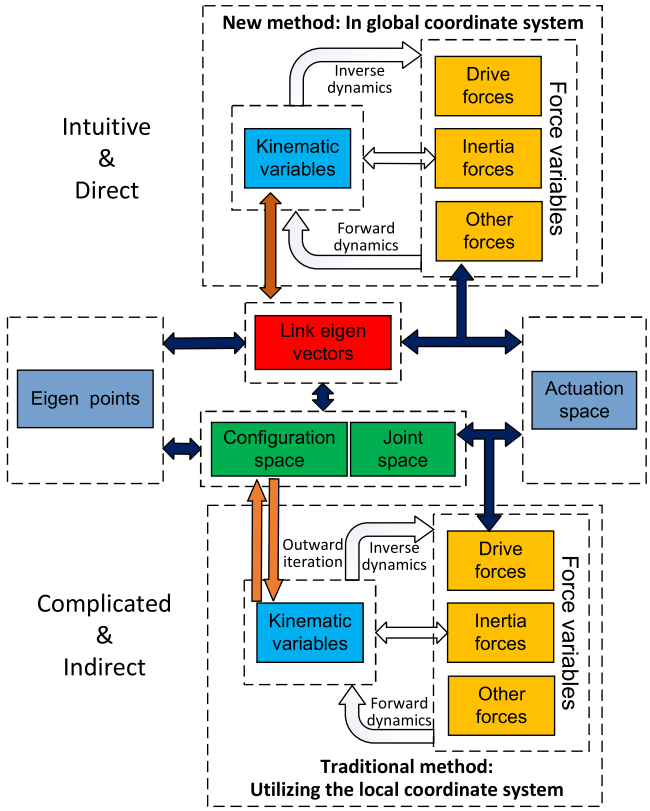

Fig. 3. Kinematic and dynamic variables' relationships.

Let n_j be the remainder of dividing j by 6, then,

$$C_{sj} = \sum_{k=1}^{k=n_{j-1}+1} s_{k,j} \quad (j = 1, 2 \cdots 18). \tag{10}$$

If the cable is tensioned, C_{sj} can be taken as the real cable's total length. Thus, the mapping is solved.

III. Dynamics

As is shown in Fig. 3, the traditional dynamic methods [23], [24], [25] solve problems with the local coordinate systems, i.e., the kinematic and dynamic variables are analyzed in the local frames or transforming the joint parameters into global variables or some other ways. Since classical mechanics is only effective in the inertial frame, the process of utilizing the local frames is complicated and indirect. Actually, for the tracking geometric curve method, all parameters can be solved in a unified inertial global frame, so the local frames and joint space can be abandoned. In this article, the Newton–Euler method is adopted and the dynamic equations are simplified with some techniques.

A. Analysis of Cable Forces

Cable forces are the driving forces for the manipulator's joints. Due to the small mass and low speed of the cables, the paper ignores the dynamics of the cables themselves.

As the lubrication between the cables and the holes is good and there is no stick-slip phenomenon, the Coulomb friction model

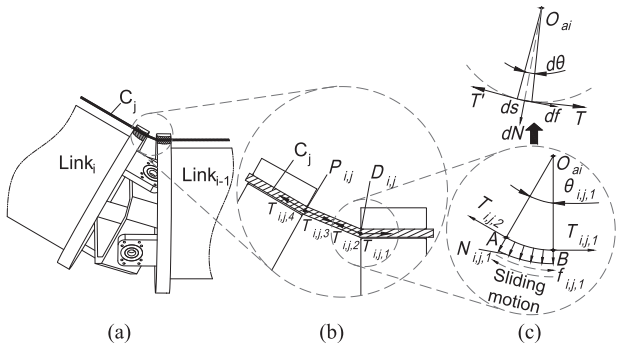

Fig. 4. Cable forces' analysis on Joint$_i$. (a) Joint$_i$. (b) $C_j's$ force on Joint$_i$. (c) Force analysis.

with continuous saturation function is adopted. The friction coefficient is,

$$\mu = \mu_0 \cdot \text{sat}\,(v_{i,j,k}) \tag{11}$$

μ_0 : Coefficient of sliding friction. Set $\mu_0 = 0.14$.
$v_{i,j,k}$: If $k = 1$, it is the velocity of C$_j$ relative to $D_{i,j}$. If $k = 2$, it is the velocity of C$_j$ relative to $P_{i,j}$. And if the cable is moved to the distal end relative to the hole, $v_{i,j,k}$ is defined as positive.
sat(): Saturation function, which is defined below,

$$\text{sat}\ (v_{i,j,k}) = \begin{cases} \text{sign}\,(v_{i,j,k}) & |k_u v_{i,j,k}| \geq 1 \\ k_u v_{i,j,k} & |k_u v_{i,j,k}| < 1 \end{cases}. \tag{12}$$

sign(): Sign function that returns the positive or negative sign.
k_u: Predefined coefficient. Set $k_u = 20\,000$.

Fig. 4(a) shows Joint$_i$, and (b) shows the force analysis of C$_j$ in Joint$_i$. There are 4 tension forces in the figure. And $\boldsymbol{T_{i,j,2}}, \boldsymbol{T_{i,j,3}}$ are equal with opposite directions, while $\boldsymbol{T_{i,j,4}}, \boldsymbol{T_{i+1,j,1}}$ are equal with opposite directions.

As is shown in Fig. 4(c), the force analysis of a cable passing through the hole is simplified as the case of a cable twining around a cylinder. Arc $\widehat{AB}$ is the contact line between the cable and $D_{i,j}$, and its contact angle is $\theta_{i,j,1}$. The cable is subjected to the distribution pressure $\boldsymbol{N_{i,j,1}}$, friction force $\boldsymbol{f_{i,j,1}}$, and tension forces $\boldsymbol{T_{i,j,1}}, \boldsymbol{T_{i,j,2}}$. Then, though Link$_{i-1}$ is subjected to $-\boldsymbol{N_{i,j,1}}$ and $-\boldsymbol{f_{i,j,1}}$ at $D_{i,j}$, the resultant force is,

$$\boldsymbol{F_{D_{i,j}}} = \boldsymbol{T_{i,j,1}} + \boldsymbol{T_{i,j,2}}. \tag{13}$$

Similarly, the resultant force on Link$_{i-1}$ from C$_j$ at $P_{i-1,j}$ is

$$\boldsymbol{F_{P_{i-1,j}}} = \boldsymbol{T_{i-1,j,3}} + \boldsymbol{T_{i-1,j,4}}. \tag{14}$$

Therefore, the total acting force on Link$_{i-1}$ from C$_j$ is

$$\boldsymbol{F_{C_{i-1,j}}} = \boldsymbol{F_{P_{i-1,j}}} + \boldsymbol{F_{D_{i,j}}} = \boldsymbol{T_{i,j,2}} + \boldsymbol{T_{i-1,j,3}}. \tag{15}$$

The infinitesimal arc element ds is cut from Arc $\widehat{AB}$, and its contact angle is $d\theta$. $\boldsymbol{T}, \boldsymbol{T'}$ are the tension forces on both ends of ds, $\boldsymbol{dN}$ is the pressure force on ds from the hole, and $\boldsymbol{df}$ is the friction force. Then,

$$\boldsymbol{T} + \boldsymbol{T'} + \boldsymbol{dN} + \boldsymbol{df} = \boldsymbol{0}. \tag{16}$$

And, $\boldsymbol{dN}, \boldsymbol{df}$ can be decomposed as follows:

$$\begin{cases} \boldsymbol{dN} = n\left(dN\right)\boldsymbol{e_n} + \tau\left(dN\right)\boldsymbol{e}_\tau \\ \boldsymbol{df} = \tau(df)\boldsymbol{e}_\tau + n\left(df\right)\boldsymbol{e_n} \end{cases} \tag{17}$$

$\boldsymbol{e_n}$: Normal direction of the arc element.
$\boldsymbol{e}_\tau$: Tangent direction of the arc element.
$n(dN)$: Value of normal component of $\boldsymbol{dN}$, set $n\left(dN\right) = dN_0$.
$\tau(dN)$: Value of tangent component of $\boldsymbol{dN}$.
$\tau(df)$: Value of tangent component of $\boldsymbol{df}$.
$n(df)$: Value of normal component of $\boldsymbol{df}$.

The variables above satisfy the following expressions:

$$\tau\ (dN) = o\left(dN_0\right) \tag{18}$$

$$\tau\ (df) = \mu dN_0 + o\ (\mu dN_0) = \mu dN_0 + o\left(dN_0\right) \tag{19}$$

$$n\ (df) = o\ (\tau\left(df\right)) = o\left(dN_0\right). \tag{20}$$

$o()$ refers to the higher order infinitesimal. Then, if (16) is projected along the tangent and normal directions, we can get,

$$\begin{cases} (T' - T)\cos\left(0.5d\theta\right) - \mu dN_0 + o\ (dN_0) = 0 \\ (-T' - T)\sin\left(0.5d\theta\right) + dN_0 + o\ (dN_0) = 0 \end{cases}. \tag{21}$$

T, T' are the value of $\boldsymbol{T}, \boldsymbol{T'}$. And as $d\theta$ is the infinitesimal

$$\begin{cases} \sin\ (0.5d\theta) = 0.5d\theta + o\left(d\theta\right) \\ \cos\left(0.5d\theta\right) = 1 + o\left(d\theta\right) \end{cases}. \tag{22}$$

Substitute the above equations into (21) and ignore the higher order infinitesimal, we can get,

$$\begin{cases} T' - T - \mu \cdot d\ N_0 = 0 \\ (-T' - T)\,0.5d\theta + d\ N_0 = 0 \end{cases}. \tag{23}$$

Then, we can get,

$$\begin{aligned} T'/T &= (1 + 0.5\mu \cdot d\theta)\,/\,(1 - 0.5\mu \cdot d\theta) \\ &= 1 + \mu \cdot d\theta + o\left(\mu \cdot d\theta\right). \end{aligned} \tag{24}$$

Therefore, we can get,

$$T_{i,j,2}/\,T_{i,j,1} = \lim_{d\theta \to 0^+} (1 + \mu \cdot d\theta)^{\theta_{i,j,1}/d\theta} = e^{\mu\theta_{i,j,1}}. \tag{25}$$

Similarly, let $\theta_{i,j,2}$ be the contact angle between $\mathrm{C_j}$ and $P_{i,j}$,

$$T_{i,j,4}/\,T_{i,j,3} = e^{\mu\theta_{i,j,2}}. \tag{26}$$

According to the positions of $P_{i-1,j}, D_{i,j}, P_{i,j}$, and $D_{i+1,j}$, we can further get the unit direction vectors of $\boldsymbol{T_{i,j,1}}, \ldots \boldsymbol{T_{i,j,4}}$,

$$\begin{cases} \boldsymbol{u_{vi,j,1}} = (P_{i-1,j} - D_{i,j}\ )/\left|D_{i,j} - P_{i-1,j}\right| \\ \boldsymbol{u_{vi,j,2}} = (P_{i,j}\ - D_{i,j})/\left|P_{i,j} - D_{i,j}\right| \\ \boldsymbol{u_{vi,j,3}} = -\boldsymbol{u_{vi,j,2}} \\ \boldsymbol{u_{vi,j,4}} = (D_{i+1,j}\ - P_{i,j})/\left|D_{i+1,j} - P_{i,j}\right| \end{cases}. \tag{27}$$

Then,

$$\begin{cases} \theta_{i,j,1} = \pi - \cos^{-1}\left(\boldsymbol{u_{vi,j,1}} \cdot \boldsymbol{u_{vi,j,2}}\right) \\ \theta_{i,j,2} = \pi - \cos^{-1}\left(\boldsymbol{u_{vi,j,3}} \cdot \boldsymbol{u_{vi,j,4}}\right) \end{cases}. \tag{28}$$

As a result, as long as the tension force at one end of the cable is known, every tension force at each section of the cable can be calculated. And then all cable forces acting on the links can be calculated through (15).

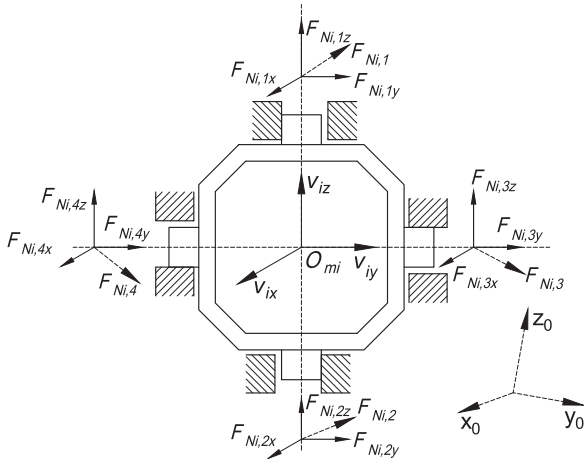

Fig. 5. Force analysis of $\mathrm{HR_i}$.

B. Analysis of Hollow Ring and Link Forces

1) Analysis of Hollow Ring Forces: $\mathrm{HR_i}$ is the key part of $\mathrm{Joint_i}$, which connects Link_{i-1} and $\mathrm{Link_i}$. There are three kinds of forces on $\mathrm{HR_i}$. The first are the acting forces from Link_{i-1} and Link_i. The second is the gravity force. The third is the inertia force.

When the bearings are distributed on two ends of a shaft, the bending moment on the shaft could be balanced by the supporting forces of the bearings at both ends. Therefore, the bearing at each end of $\mathrm{HR_i}$ would only have supporting forces on the shaft, but no bending moment. Additionally, since the friction force at each revolute pair is negligible with good lubrication, the torque moments can also be ignored. Thus, the first kind of forces at each bearing of $\mathrm{HR_i}$ have no moment, which are shown in Fig. 5. And the forces from $\mathrm{Link_i}$ are $\boldsymbol{F_{Ni,1}}, \boldsymbol{F_{Ni,2}}$, the forces from Link_{i-1} are $\boldsymbol{F_{Ni,3}}, \boldsymbol{F_{Ni,4}}$. Furtherly, $\boldsymbol{F_{Ni,1}} \cdots \boldsymbol{F_{Ni,4}}$ can be decomposed along the $\mathrm{HR_i}$'s eigenvectors, $\boldsymbol{F_{Ni,1x}}, \boldsymbol{F_{Ni,1y}}, \boldsymbol{F_{Ni,1z}}, \boldsymbol{F_{Ni,2x}}, \cdots \boldsymbol{F_{Ni,4x}}, \boldsymbol{F_{Ni,4y}}$, $\boldsymbol{F_{Ni,4z}}$. Since $\boldsymbol{F_{Ni,1z}}, \boldsymbol{F_{Ni,2z}}$ act on the same line, they can be merged as one, $\boldsymbol{F_{Ni,zc}}$. Similarly, $\boldsymbol{F_{Ni,3y}}, \boldsymbol{F_{Ni,4y}}$ can be merged as $\boldsymbol{F_{Ni,yc}}$. Then, the acting forces on $\mathrm{HR_i}$ from adjacent links are as follows:

$$\begin{aligned} \boldsymbol{F_{Hi}} = \sum_{n=1}^{4} \boldsymbol{F_{Ni,nx}} &+ \boldsymbol{F_{Ni,1y}} + \boldsymbol{F_{Ni,2y}} + \boldsymbol{F_{Ni,yc}} \\ &+ \boldsymbol{F_{Ni,zc}} + \boldsymbol{F_{Ni,3z}} + \boldsymbol{F_{Ni,4z}}. \end{aligned} \tag{29}$$

The gravity of $\mathrm{HR_i}$ is

$$\boldsymbol{G_H} = m_H\,\boldsymbol{g} = -m_H g\boldsymbol{u_{0z}} = [00\ -m_H g]^T \tag{30}$$

m_H : Mass of $\mathrm{HR_i}$, and the mass of every hollow ring is equal.
$\boldsymbol{g}$: Gravity acceleration.

$\mathrm{HR_i}$'s inertia force's solving needs the kinematic variables, which are calculated through $\mathrm{HR_i}$'s eigenvectors and O_{mi}'s position. In this article, the discrete control is adopted. And since the cycle time is short enough, the discrete kinematic

variables, including velocity, acceleration, angular velocity and angular acceleration, are approximately equal to the continuous kinematic variables. Thus, the inertia force can be calculated with the discrete variables.

The velocity of $\mathrm{HR_i}$'s centroid at current period is

$$\boldsymbol{v_{cH,i}} = \left(O_{mi} - O'_{mi}\right)/\Delta T. \tag{31}$$

O_{mi} : Position of $\mathrm{HR_i}$'s centroid at the current period, which is also the proximal end of Link_i.
O'_{mi} : Position of $\mathrm{HR_i}$'s centroid at last period.
ΔT : Cycle time. Set $\Delta T = 10$ ms.

Then, the acceleration of $\mathrm{HR_i}$'s centroid at current period is

$$\boldsymbol{a_{ccH,i}} = \left(\boldsymbol{v_{cH,i}} - \boldsymbol{v_{cH,i}}'\right)/\Delta T \tag{32}$$

$\boldsymbol{v_{cH,i'}}$: Velocity of $\mathrm{HR_i}$'s centroid at last period.

Then, the inertia force on $\mathrm{HR_i}$ is

$$\boldsymbol{F_{IH,i}} = -m_H \cdot \boldsymbol{a_{ccH,i}}. \tag{33}$$

In order to calculate the angular velocity $\boldsymbol{\omega_{Hi}}$ and the angular acceleration $\boldsymbol{\alpha_{Hi}}$, let

$$\begin{cases} \dot{\boldsymbol{v}}_{\boldsymbol{iy}} = \left(\boldsymbol{v_{iy}} - \boldsymbol{v_{iy'}}\right)/\Delta T \\ \dot{\boldsymbol{v}}_{\boldsymbol{iz}} = \left(\boldsymbol{v_{iz}} - \boldsymbol{v_{iz}}'\right)/\Delta T \end{cases} \tag{34}$$

$\boldsymbol{v_{iy'}}, \boldsymbol{v_{iz'}}$: Two eigenvectors of $\mathrm{HR_i}$ at last period.

If $\dot{\boldsymbol{v}}_{\boldsymbol{iz}} \times \dot{\boldsymbol{v}}_{\boldsymbol{iy}} = \boldsymbol{0}$, the angular velocity of $\mathrm{HR_i}$ is

$$\boldsymbol{\omega_{Hi}} = \begin{cases} \boldsymbol{0} & if \dot{\boldsymbol{v}}_{\boldsymbol{iy}} = \dot{\boldsymbol{v}}_{\boldsymbol{iz}} = \boldsymbol{0} \\ |\dot{\boldsymbol{v}}_{\boldsymbol{iz}}| \cdot \boldsymbol{v_{iy}} & if \dot{\boldsymbol{v}}_{\boldsymbol{iy}} = \boldsymbol{0} \\ |\dot{\boldsymbol{v}}_{\boldsymbol{iy}}| \cdot \boldsymbol{v_{iz}} & if\ \dot{\boldsymbol{v}}_{\boldsymbol{iz}} = \boldsymbol{0} \end{cases}. \tag{35}$$

If $\dot{\boldsymbol{v}}_{\boldsymbol{iz}} \times \dot{\boldsymbol{v}}_{\boldsymbol{iy}} \neq \boldsymbol{0}$, let

$$\boldsymbol{\omega_0} = \left(\dot{\boldsymbol{v}}_{\boldsymbol{iz}} \times \dot{\boldsymbol{v}}_{\boldsymbol{iy}}\right) / \left|\dot{\boldsymbol{v}}_{\boldsymbol{iz}} \times \dot{\boldsymbol{v}}_{\boldsymbol{iy}}\right|. \tag{36}$$

Then, the angular velocity of $\mathrm{HR_i}$ is

$$\boldsymbol{\omega_{Hi}} = |\dot{\boldsymbol{v}}_{\boldsymbol{iz}}|^2 \boldsymbol{\omega_0} / \left(\dot{\boldsymbol{v}}_{\boldsymbol{iz}} \cdot \left(\boldsymbol{\omega_0} \times \boldsymbol{v_{iz}}\right)\right). \tag{37}$$

Then, the angular acceleration of $\mathrm{HR_i}$ is

$$\boldsymbol{\alpha_{Hi}} = \left(\boldsymbol{\omega_{Hi}} - \boldsymbol{\omega_{Hi}}'\right)/\Delta T \tag{38}$$

$\boldsymbol{\omega_{Hi}}'$: Angular velocity of $\mathrm{HR_i}$ at last period.

Let $\boldsymbol{I_{cH}}$ be the inertia tensor of $\mathrm{HR_i}$ relative to the center of mass, which is calculated in the local coordinate system. The local coordinate system is defined as: Set $\mathrm{HR_i}$'s eigenvectors as x-, y-, and z-axes, and O_{mi} as the origin. Then $\boldsymbol{I_{cH}}$ is constant and can be solved in advance according to the mass distribution of the hollow ring. $\boldsymbol{I_{cH}}$ is defined as

$$\boldsymbol{I_{cH}} = \int \left(|\boldsymbol{r}|^2 \boldsymbol{I}_3 - \boldsymbol{r}\boldsymbol{r}^{\boldsymbol{T}}\right) dm \tag{39}$$

dm: Mass element of $\mathrm{HR_i}$.
$\boldsymbol{r}$: Vector from mass element to the centroid of $\mathrm{HR_i}$ in the local coordinate system.
$\boldsymbol{I}_3$: Identity matrix with 3-order.

Let $\boldsymbol{r_0}$ be the vector from mass element to the centroid of $\mathrm{HR_i}$ in the global coordinate system, then

$$\boldsymbol{r_0} = \left[\boldsymbol{v_{ix}}\ \boldsymbol{v_{iy}}\ \boldsymbol{v_{iz}}\right]\ \boldsymbol{r}. \tag{40}$$

Set $\boldsymbol{R_i} = \left[\boldsymbol{v_{ix}}\ \boldsymbol{v_{iy}}\ \boldsymbol{v_{iz}}\right]$, then the inertia tensor of $\mathrm{HR_i}$ in the global coordinate system is

$$\begin{aligned} \boldsymbol{I_{cH,i}} &= \int \left(|\boldsymbol{r_0}|^2 \boldsymbol{I}_3 - \boldsymbol{r_0}\boldsymbol{r_0^T}\right) dm \\ &= \int \left[\left(\boldsymbol{r^T r}\right) \boldsymbol{R_i}\boldsymbol{R_i^T} - \boldsymbol{R_i}\boldsymbol{r}\boldsymbol{r}^T\boldsymbol{R_i^T}\right] dm \\ &= \boldsymbol{R_i} \int \left(|\boldsymbol{r}|^2 \boldsymbol{I}_3 - \boldsymbol{r}\boldsymbol{r}^{\boldsymbol{T}}\right) dm \boldsymbol{R_i^T} = \boldsymbol{R_i}\boldsymbol{I_{cH}}\boldsymbol{R_i^T}. \end{aligned} \tag{41}$$

In the global coordinate system, the inertia moment on $\mathrm{HR_i}$ about the centroid is

$$\begin{aligned} \boldsymbol{M_{IH,i}} &= -d\left(\boldsymbol{I_{cH,i}}\boldsymbol{\omega_{Hi}}\right)/dt \\ &= -\boldsymbol{I_{cH,i}}\boldsymbol{\alpha_{Hi}} - \boldsymbol{\omega_{Hi}} d\boldsymbol{I_{cH,i}}/dt. \end{aligned} \tag{42}$$

Substitute (41) into (42), we get

$$d\boldsymbol{I_{cH,i}}/dt = \dot{\boldsymbol{R}}_{\boldsymbol{\iota}}\boldsymbol{I_{cH}}\boldsymbol{R_i^T} + \boldsymbol{R_i}\boldsymbol{I_{cH}}\dot{\boldsymbol{R}}_{\boldsymbol{i}}^{\boldsymbol{T}}. \tag{43}$$

Let $\boldsymbol{\omega_{Hi}} = \left[\omega_{Hi,x}, \omega_{Hi,y}, \omega_{Hi,z}\right]^T$, then its corresponding skew symmetric cross product matrix is

$$\mathrm{Sk}\ \left(\boldsymbol{\omega_{Hi}}\right) = \begin{bmatrix} 0 & -\omega_{Hi,z} & \omega_{Hi,y} \\ \omega_{Hi,z} & 0 & -\omega_{Hi,x} \\ -\omega_{Hi,y} & \omega_{Hi,x} & 0 \end{bmatrix}. \tag{44}$$

Then, the time derivative of the rotation matrix is

$$\dot{\boldsymbol{R}}_{\boldsymbol{\iota}} = \boldsymbol{\omega_{Hi}} \times \boldsymbol{R_i} = \mathrm{Sk}\left(\boldsymbol{\omega_{Hi}}\right)\boldsymbol{R_i}. \tag{45}$$

Then, (43) can be transformed into

$$\begin{aligned} \frac{d\boldsymbol{I_{cH,i}}}{dt} &= \mathrm{Sk}\left(\boldsymbol{\omega_{Hi}}\right)\boldsymbol{R_i}\boldsymbol{I_{cH}}\boldsymbol{R_i^T} + \boldsymbol{R_i}\boldsymbol{I_{cH}}\boldsymbol{R_i^T}\mathrm{Sk}^{\mathrm{T}}\left(\boldsymbol{\omega_{Hi}}\right) \\ &= \mathrm{Sk}\left(\boldsymbol{\omega_{Hi}}\right)\boldsymbol{I_{cH,i}} - \boldsymbol{I_{cH,i}}\mathrm{Sk}\left(\boldsymbol{\omega_{Hi}}\right). \end{aligned} \tag{46}$$

Then,

$$\begin{aligned} &\left(\frac{d\boldsymbol{I_{cH,i}}}{dt}\right)\boldsymbol{\omega_{Hi}} \\ &= \mathrm{Sk}\left(\boldsymbol{\omega_{Hi}}\right)\boldsymbol{I_{cH,i}}\boldsymbol{\omega_{Hi}} - \boldsymbol{I_{cH,i}}\mathrm{Sk}\left(\boldsymbol{\omega_{Hi}}\right)\ \boldsymbol{\omega_{Hi}} \\ &= \boldsymbol{\omega_{Hi}} \times \left(\boldsymbol{I_{cH,i}}\boldsymbol{\omega_{Hi}}\right) - \boldsymbol{I_{cH,i}}\left(\boldsymbol{\omega_{Hi}} \times \boldsymbol{\omega_{Hi}}\right) \\ &= \boldsymbol{\omega_{Hi}} \times \left(\boldsymbol{I_{cH,i}}\boldsymbol{\omega_{Hi}}\right). \end{aligned} \tag{47}$$

Then, substitute (47) into (42), the inertia moment is

$$\boldsymbol{M_{IH,i}} = -\boldsymbol{I_{cH,i}}\boldsymbol{\alpha_{Hi}} - \boldsymbol{\omega_{Hi}} \times \left(\boldsymbol{I_{cH,i}}\boldsymbol{\omega_{Hi}}\right). \tag{48}$$

As the hollow ring's mass and inertia tensor are small, its dynamics sometimes can be ignored for calculation efficiency.

2) Analysis of Link Forces: There are five kinds of forces on $\mathrm{Link_i}$. The first are the cable forces. The second are the acting forces from adjacent hollow rings. The third are the environment forces. The fourth is the gravity force. The fifth is the inertia force. Fig. 6 shows the first and second kind of forces on $\mathrm{Link_4}$.

The first kind of forces acting on $\mathrm{Link_i}$ can be divided into the known cable forces and the driving forces. The known cable forces are from the cables passing through $\mathrm{Link_i}$, which are fixed on $\mathrm{Link_m}(m > i)$. Since $\mathrm{Link_m}$'s force analysis is done before $\mathrm{Link_i}$'s, $\boldsymbol{T}_{m,m,3}, \boldsymbol{T}_{m,m+6,3}, \boldsymbol{T}_{m,m+12,3}$ are all known parameters. Thus, the tension forces on every section of $\mathrm{C_m}$,

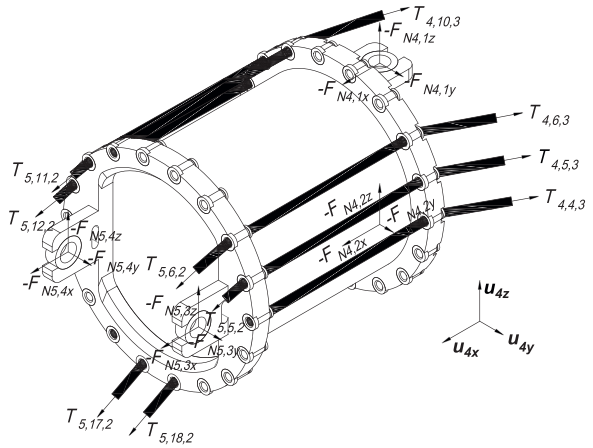

Fig. 6. Force analysis of Link$_i$.

C_{m+6}, C_{m+12} can be solved according to (25) and (26). Then, the known cable forces can be calculated as

$$\begin{aligned}\boldsymbol{S_{T1,i}} &= \sum_{j=i+1}^{j=6} \boldsymbol{F_{C_{i,j}}} + \sum_{j=i+7}^{j=12} \boldsymbol{F_{C_{i,j}}} + \sum_{j=i+13}^{j=18} \boldsymbol{F_{C_{i,j}}} \\ &= \sum_{j=i+1}^{j=6} (\boldsymbol{T_{i+1,j,2}} + \boldsymbol{T_{i,j,3}}) \\ &\quad + \sum_{j=i+7}^{j=12} (\boldsymbol{T_{i+1,j,2}} + \boldsymbol{T_{i,j,3}}) \\ &\quad + \sum_{j=i+13}^{j=18} (\boldsymbol{T_{i+1,j,2}} + \boldsymbol{T_{i,j,3}}). \end{aligned} \tag{49}$$

The driving forces are unknown and to be solved. They are from the cables C_j $(j = i, j = i + 6, j = i + 12)$, which are fixed on Link$_i$. Since $\boldsymbol{T_{i+1,j,2}}$ actually is the internal force of Link$_i$, the resultant force from C_j on Link$_i$ is only $\boldsymbol{T_{i,j,3}}$. Then, the driving forces are as follows:

$$\boldsymbol{S_{T2,i}} = \boldsymbol{T_{i,i,3}} + \boldsymbol{T_{i,i+6,3}} + \boldsymbol{T_{i,i+12,3}}. \tag{50}$$

The acting forces on Link$_i$ from HR$_i$ and HR$_{i+1}$ are

$$\begin{aligned}\boldsymbol{F_{Ni}} = &-(\boldsymbol{F_{Ni,1x}} + \boldsymbol{F_{Ni,2x}} + \boldsymbol{F_{N(i+1),3x}} \\ &+ \boldsymbol{F_{N(i+1),4x}} + \boldsymbol{F_{Ni,zc}} \\ &+ \boldsymbol{F_{N(i+1),3z}} + \boldsymbol{F_{N(i+1),4z}} + \boldsymbol{F_{Ni,1y}} + \boldsymbol{F_{Ni,2y}} \\ &+ \boldsymbol{F_{N(i+1),yc}}). \end{aligned} \tag{51}$$

When $i = 6$, Link$_i$ is the end link. Then, $\boldsymbol{F_{N(i+1),3x}} + \boldsymbol{F_{N(i+1),4x}} + \boldsymbol{F_{N(i+1),3z}} + \boldsymbol{F_{N(i+1),4z}} + \boldsymbol{F_{N(i+1),yc}}$ can be treated as the environment forces. In addition, the middle links are also subjected to the environment forces, which can be from the outside and inside of the manipulator. Although the environment influence is not analyzed here, the corresponding forces can still be added into dynamics equations if necessary.

The gravity force on Link$_i$ not only comes from the link itself, but also the water pipe, gas pipe, cables, etc. For the end link, the operation tools even need to be considered. Link$_i$'s total gravity is

$$\boldsymbol{G_i} = m_i \boldsymbol{g} = -m_i g \boldsymbol{u_{0z}} = [00 - m_i g]^T \tag{52}$$

m_i : Total mass of Link$_i$.

On the analogy of HR$_i$, the inertia force on Link$_i$ is

$$\boldsymbol{F_{I,i}} = -m_i \cdot \boldsymbol{a_{cc,i}} \tag{53}$$

$\boldsymbol{a_{cc,i}}$: Acceleration of Link$_i$'s centroid at current period.

$$\boldsymbol{a_{cc,i}} = (\boldsymbol{v_{c,i}} - \boldsymbol{v_{c,i}}') / \Delta T \tag{54}$$

$\boldsymbol{v_{c,i}}$: Velocity of Link$_i$'s centroid at current period.
$\boldsymbol{v_{c,i}}'$: Velocity of Link$_i$'s centroid at last period.

Let P_{ci} be the position of Link$_i$'s centroid at current period and its value is,

$$P_{ci} = O_{mi} + a_i \boldsymbol{u_{ix}} + b_i \boldsymbol{u_{iy}} + c_i \boldsymbol{u_{iz}} \tag{55}$$

a_i, b_i, c_i: Position coefficients of Link$_i$'s centroid, which are related to the mass distribution.

$$\boldsymbol{v_{c,i}} = (P_{ci} - P_{ci}') / \Delta T \tag{56}$$

P_{ci}': Position of Link$_i$'s centroid at last period.

The inertia moment on Link$_i$ about the centroid is,

$$\boldsymbol{M_{I,i}} = -\boldsymbol{I_{c,i}} \boldsymbol{\alpha_i} - \boldsymbol{\omega_i} \times (\boldsymbol{I_{c,i}} \boldsymbol{\omega_i}) \tag{57}$$

$\boldsymbol{I_{c,i}}$: Inertia tensor of Link$_i$ in the global coordinate system.
$\boldsymbol{\omega_i}$: Angular velocity of Link$_i$.
$\boldsymbol{\alpha_i}$: Angular acceleration of Link$_i$.

The calculations of $\boldsymbol{I_{c,i}}, \boldsymbol{\omega_i}, \boldsymbol{\alpha_i}$ are similar to the calculation of $\boldsymbol{I_{cH,i}}, \boldsymbol{\omega_{Hi}}, \boldsymbol{\alpha_{Hi}}$.

C. Inverse Dynamics Method

The traditional Newton–Euler method includes outward and inward iterations. Outward iteration solves the kinematic parameters, while the inward iteration solves the driving forces. In the tracking geometric curve method, the traditional dynamics would figure out the joint parameters and their first and second derivatives first based on the known manipulator's eigenpoints, and then the kinematic parameters of the links. That not only wastes the convenience of the geometric method to solve the kinematic parameters in the global coordinate system but also makes the dynamic description cumbersome and complicated. Thus, the dynamic model in this article makes the calculation from manipulator's eigenpoints to kinematic parameters more direct. As is shown in Section III–B, the inertia forces of Link$_i$ and HR$_i$ are already calculated from the global kinematic parameters, so the desired solution of the outward iteration has already been done. Additionally, compared to the joint parameters, link eigenvectors are more intuitive and easier to be obtained. The following text will demonstrate the inverse dynamics in detail.

1) Method for Setting the Optimal Driving Forces: The driving forces of the CSM is from the cables. Since each universal joint with 2 DOFs is driven by three cables, it belongs to the redundant actuation. The ith recursive Newton–Euler equations

have 12 independent equations involving $\mathrm{HR_i}$ and $\mathrm{Link_i}$. And the unknown vectors in the equations include 3 driving forces, $\boldsymbol{T_{i,i,3}}, \boldsymbol{T_{i,i+6,3}}, \boldsymbol{T_{i,i+12,3}}$, 5 interaction forces between $\mathrm{HR_i}$ and $\mathrm{Link_i}$, $\boldsymbol{F_{Ni,1x}}, \boldsymbol{F_{Ni,2x}}, \boldsymbol{F_{Ni,zc}}, \boldsymbol{F_{Ni,1y}}, \boldsymbol{F_{Ni,2y}}$, and 5 interaction forces between $\mathrm{Link_{i-1}}$ and $\mathrm{HR_i}$, $\boldsymbol{F_{Ni,3x}}, \boldsymbol{F_{Ni,4x}}, \boldsymbol{F_{Ni,3z}}, \boldsymbol{F_{Ni,4z}}, \boldsymbol{F_{Ni,yc}}$. Since the directions of these vectors are known, the 12 independent equations have 13 unknown variables, which also means the actuation is redundant. Thus, for a better dynamic effect, it is meaningful to set the optimal driving forces. The goals are as follows.

1) Driving forces are greater than the pretensioning force T_{pre}, which promises the accuracy and stiffness of the CSM.
2) The cable forces, not only the maximum cable force but every cable force, should be as small as possible.

Although the optimal driving forces can be obtained by the setting and solving of the optimal objective function, it only needs to set the minimum of $\mathrm{Joint_i}$'s 3 driving forces equal to T_{pre}. The proof is as follows.

Let $\boldsymbol{S_{MT1,i}}$ be the resultant moment of the known cable forces on $\mathrm{Link_i}$ about O_{mi}, $\boldsymbol{S_{MT2,i}}$ be the resultant moment of the driving forces on $\mathrm{Link_i}$ about O_{mi}, $\boldsymbol{M_{G_i}}$ be the moment of $\boldsymbol{G_i}$ about O_{mi}, and $\boldsymbol{M_{F_{I,i}}}$ be the moment of $\boldsymbol{F_{I,i}}$ about O_{mi}, $\boldsymbol{M_{F_{Ni,k}}}$ $(k = 1, 2, 3, 4)$ be the moment of $\boldsymbol{F_{Ni,k}}$ about O_{mi}, $\boldsymbol{M_{F_{N(i+1),k}}}'$ $(k = 1, 2, 3, 4)$ be the moment of $\boldsymbol{F_{N(i+1),k}}$ about O_{mi}. When $\mathrm{Link_i}$ is the end link, $\boldsymbol{M_{F_{N(i+1),k}}}'$ means the moment of environment force about O_{mi}. Then, let $\boldsymbol{M_{1,2}} = \boldsymbol{M_{F_{Ni,1}}} + \boldsymbol{M_{F_{Ni,2}}}$, $\boldsymbol{M_{3,4}} = \boldsymbol{M_{F_{Ni,3}}} + \boldsymbol{M_{F_{Ni,4}}}$, $\boldsymbol{M_{3,4}}' = \boldsymbol{M_{F_{N(i+1),3}}}' + \boldsymbol{M_{F_{N(i+1),4}}}'$, the moment equations about O_{mi} of $\mathrm{Link_i}$, $\mathrm{HR_i}$ are as follows:

$$\begin{cases} \boldsymbol{S_{MT2,i}} - \boldsymbol{M_{1,2}} = \boldsymbol{M_{3,4}}' - \boldsymbol{M_{I,i}} - \boldsymbol{S_{MT1,i}} \\ -\boldsymbol{M_{G_i}} - \boldsymbol{M_{F_I}}, \boldsymbol{i} \\ \boldsymbol{M_{1,2}} + \boldsymbol{M_{3,4}} = -\boldsymbol{M_{IH,i}} \end{cases}. \tag{58}$$

The left side of (58) includes the unknown variables, while the right side is with the known variables. Except for $\boldsymbol{M_{I,i}}$ and $\boldsymbol{M_{IH,i}}$ whose expressions are already known, the other variables in (58) are expressed as follows:

$$\begin{aligned} &\boldsymbol{S_{MT1,i}} \\ &= \sum_{j=i+1}^{j=6} \boldsymbol{d_{i+1,j}} \times \boldsymbol{T_{i+1,j,2}} + \sum_{j=i+1}^{j=6} \boldsymbol{p_{i,j}} \times \boldsymbol{T_{i,j,3}} \\ &\quad + \sum_{j=i+7}^{j=12} \boldsymbol{d_{i+1,j}} \times \boldsymbol{T_{i+1,j,2}} + \sum_{j=i+7}^{j=12} \boldsymbol{p_{i,j}} \times \boldsymbol{T_{i,j,3}} \\ &\quad + \sum_{j=i+13}^{j=18} \boldsymbol{d_{i+1,j}} \times \boldsymbol{T_{i+1,j,2}} + \sum_{j=i+13}^{j=18} \boldsymbol{p_{i,j}} \times \boldsymbol{T_{i,j,3}} \end{aligned} \tag{59}$$

$\boldsymbol{d_{i+1,j}}$: Vector from O_{mi} to $D_{i+1,j}$.
$\boldsymbol{p_{i,j}}$: Vector from O_{mi} to $P_{i,j}$.

The values of $\boldsymbol{d_{i+1,j}}$ and $\boldsymbol{p_{i,j}}$ are as follows:

$$\begin{cases} \boldsymbol{d_{i+1,j}} = D_{i+1,j} - O_{mi} \\ \boldsymbol{p_{i,j}} = P_{i,j} - O_{mi} \end{cases}. \tag{60}$$

$\boldsymbol{S_{MT2,i}}$ contains 3 unknown variables, $T_{i,i,3}, T_{i,i+6,3}$, and $T_{i,i+12,3}$. It can be expressed as follows:

$$\begin{aligned} &\boldsymbol{S_{MT2,i}} \\ &= \boldsymbol{p_{i,i}} \times \boldsymbol{T_{i,i,3}} + \boldsymbol{p_{i,i+6}} \times \boldsymbol{T_{i,i+6,3}} \\ &\quad + \boldsymbol{p_{i,i+12}} \times \boldsymbol{T_{i,i+12,3}} \\ &= T_{i,i,3} \cdot \boldsymbol{p_{i,i}} \times \boldsymbol{u_{vi,i,3}} + T_{i,i+6,3} \cdot \boldsymbol{p_{i,i+6}} \times \boldsymbol{u_{vi,i+6,3}} \\ &\quad + T_{i,i+12,3} \cdot \boldsymbol{p_{i,i+12}} \times \boldsymbol{u_{vi,i+12,3}}. \end{aligned} \tag{61}$$

The expression of $\boldsymbol{M_{F_{Ni,k}}}$ needs to be transformed for reducing the number of unknown variables of (58). Let $\boldsymbol{R_k}$ be the vector from O_{mi} to the acting point of $\boldsymbol{F_{Ni,k}}$, then,

$$\begin{aligned} &\boldsymbol{R_1} \times \boldsymbol{F_{Ni,1x}} + \boldsymbol{R_2} \times \boldsymbol{F_{Ni,2x}} = \boldsymbol{R_1} \times \boldsymbol{F_{Ni,1x}} \\ &\quad - \boldsymbol{R_1} \times \boldsymbol{F_{Ni,2x}} \\ &= \boldsymbol{R_1} \times (\boldsymbol{F_{Ni,1x}} - \boldsymbol{F_{Ni,2x}}) = (F_{Ni,1x} - F_{Ni,2x}) \\ &\quad \boldsymbol{R_1} \times \boldsymbol{v_{ix}}. \end{aligned} \tag{62}$$

Similarly,

$$\boldsymbol{R_1} \times \boldsymbol{F_{Ni,1y}} + \boldsymbol{R_2} \times \boldsymbol{F_{Ni,2y}} = (F_{Ni,1y} - F_{Ni,2y})\, \boldsymbol{R}_1 \times \boldsymbol{v_{iy}} \tag{63}$$

$$\boldsymbol{R_3} \times \boldsymbol{F_{Ni,3x}} + \boldsymbol{R_4} \times \boldsymbol{F_{Ni,4x}} = (F_{Ni,3x} - F_{Ni,4x})\, \boldsymbol{R_3} \times \boldsymbol{v_{ix}} \tag{64}$$

$$\boldsymbol{R_3} \times \boldsymbol{F_{Ni,3z}} + \boldsymbol{R_4} \times \boldsymbol{F_{Ni,4z}} = (F_{Ni,3z} - F_{Ni,4z})\, \boldsymbol{R_3} \times \boldsymbol{v_{iz}}. \tag{65}$$

Let,

$$\begin{cases} x_{i,1} = F_{Ni,1x} - F_{Ni,2x} \\ x_{i,2} = F_{Ni,1y} - F_{Ni,2y} \\ x_{i,3} = F_{Ni,3x} - F_{Ni,4x} \\ x_{i,4} = F_{Ni,3z} - F_{Ni,4z} \end{cases}. \tag{66}$$

Then,

$$\begin{aligned} \boldsymbol{M_{1,2}} &= \boldsymbol{R_1} \times (\boldsymbol{F_{Ni,1x}} + \boldsymbol{F_{Ni,1y}} + \boldsymbol{F_{Ni,1z}}) + \boldsymbol{R_2} \\ &\quad \times (\boldsymbol{F_{Ni,2x}} + \boldsymbol{F_{Ni,2y}} + \boldsymbol{F_{Ni,2z}}) \\ &= \boldsymbol{R_1} \times (\boldsymbol{F_{Ni,1x}} + \boldsymbol{F_{Ni,1y}}) + \boldsymbol{R_2} \\ &\quad \times (\boldsymbol{F_{Ni,2x}} + \boldsymbol{F_{Ni,2y}}) \\ &= x_{i,1} \cdot \boldsymbol{R_1} \times \boldsymbol{v_{ix}} + x_{i,2} \cdot \boldsymbol{R_1} \times \boldsymbol{v_{iy}}. \end{aligned} \tag{67}$$

Similarly,

$$\boldsymbol{M_{3,4}} = x_{i,3} \cdot \boldsymbol{R_3} \times \boldsymbol{v_{ix}} + x_{i,4} \cdot \boldsymbol{R_3} \times \boldsymbol{v_{iz}} \tag{68}$$

And the value of $\boldsymbol{M_{F_{N(i+1),k}}}'$ is

$$\boldsymbol{M_{F_{N(i+1),k}}}' = \boldsymbol{R_k}' \times \boldsymbol{F_{N(i+1),k}} \tag{69}$$

$\boldsymbol{R_k}'$: Vector from O_{mi} to the acting point of $\boldsymbol{F_{N(i+1),k}}$.

The value of $\boldsymbol{M_{G_i}}$ is

$$\boldsymbol{M_{G_i}} = \boldsymbol{p_{cOmi}} \times \boldsymbol{G_i} \tag{70}$$

$\boldsymbol{p_{cOmi}}$: Vector from O_{mi} to $\mathrm{Link_i}$'s centroid.

The value of $\boldsymbol{M_{F_{I,i}}}$ is (Note the difference between $\boldsymbol{M_{F_{I,i}}}$ and $\boldsymbol{M_{I,i}}$.)

$$\boldsymbol{M_{F_{I,i}}} = \boldsymbol{p_{cOmi}} \times \boldsymbol{F_{I,i}}. \tag{71}$$

Finally, $T_{i,i,3}, T_{i,i+6,3}, T_{i,i+12,3}, x_{i,1}, x_{i,2}, x_{i,3}, x_{i,4}$ are the 7 unknown variables of (58). Let $\boldsymbol{X_n} = T_{i,n,3} \cdot \boldsymbol{p_{i,n}} \times \boldsymbol{u_{vi,n,3}}$, then $\boldsymbol{S_{MT2,i}} = \boldsymbol{X_i} + \boldsymbol{X_{i+6}} + \boldsymbol{X_{i+12}}$. Let $\boldsymbol{M_{Omi}} = \boldsymbol{M'_{3,4}} - \boldsymbol{M_{I,i}} - \boldsymbol{S_{MT1,i}} - \boldsymbol{M_{G_i}} - \boldsymbol{M_{F_{I,i}}}$ and move $\boldsymbol{X_i}$, one term of $\boldsymbol{S_{MT2,i}}$ in the first equation of (58), to the right side, (58) can be transformed to

$$\begin{cases} \boldsymbol{X_{i+6}} + \boldsymbol{X_{i+12}} - \boldsymbol{M_{1,2}} = \boldsymbol{M_{Omi}} - \boldsymbol{X_i} \\ \boldsymbol{M_{1,2}} + \boldsymbol{M_{3,4}} = -\boldsymbol{M_{IH,i}} \end{cases}. \tag{72}$$

The right part of the equations can be expressed as

$$B = -T_{i,i,3} \cdot [\boldsymbol{p_{i,j}} \times \boldsymbol{u_{vi,i,3}} \boldsymbol{000}]^{\boldsymbol{T}} + [\boldsymbol{M_{Omi}} (-\boldsymbol{M_{IH,i}})]^{\boldsymbol{T}}. \tag{73}$$

And let D be the coefficient matrix of (72), then

$$\begin{aligned} T_{i,i+6,3} &= |D_1| / |D| = (T_{i,i,3}|D_X| + |D_Y|) / |D| \\ &= k_1 T_{i,i,3} + c_1 \end{aligned} \tag{74}$$

D_1 : Matrix obtained by replacing the first column of D with B.
D_X: Matrix obtained by replacing the first column of D with $-[\boldsymbol{p_{i,j}} \times \boldsymbol{u_{vi,i,3}} \boldsymbol{000}]^{\boldsymbol{T}}$.
D_Y: Matrix obtained by replacing the first column of D with $[\boldsymbol{M_{Omi}}(-\boldsymbol{M_{IH,i}})]^{\boldsymbol{T}}$.

Coefficients k_1, c_1 are defined for convenient description

$$\begin{cases} k_1 = |D_X| / |D| \\ c_1 = |D_Y| / |D| \end{cases}. \tag{75}$$

Similarly, k_2, c_2 can also be defined. Thus,

$$T_{i,i+12,3} = k_2 T_{i,i,3} + c_2. \tag{76}$$

Next, we will prove k_1 is positive in any reasonable case. Set $\boldsymbol{P_{ix}}$ as the projection of $\boldsymbol{u_{ix}}$ in the plane determined by $\boldsymbol{u_{(i-1)y}}$ and $\boldsymbol{u_{(i-1)z}}$. Let φ be the included angle between $\boldsymbol{P_{ix}}$ and $\boldsymbol{u_{(i-1)y}}$, γ be the included angle between $\boldsymbol{u_{ix}}$ and $\boldsymbol{u_{(i-1)x}}$. Actually, γ reflects the bending degree of the CSM and $\gamma \leq 0.2\pi$. $P_{i,i}$ is the hole on $\text{Disc}_{2,\text{i}}$, which is passed through by the cable C_i. Let Ψ be the included angle between $\overrightarrow{O_{bi}P_{i,i}}$ and $\overrightarrow{O_{bi}P_{i,1}}$. When Ψ traverses from 0 to 2π, φ traverses from 0 to 2π and γ traverses from 0 to 0.2π, the value of k_1 has been calculated for all cases. Fig. 7(a) shows the relation among φ, γ and k_1 when $\Psi = 2\pi$. Fig. 7(b) shows the relation among φ, γ and k_2 when $\Psi = 0.5\pi$. The result shows k_1 is always greater than 0, i.e., $T_{i,i,3}, T_{i,i+6,3}$ are positively correlated. And since $T_{i,i,3}, T_{i,i+6,3}, T_{i,i+12,3}$ are rotationally symmetric, they are all positively correlated, which means all increase when one increases, and all decrease when one decreases.

As a result, when the minimum of $T_{i,i,3}, T_{i,i+6,3}, T_{i,i+12,3} (i = 1, 2 \cdots 6)$ is equal to T_{pre}, the two goals of setting the optimal driving forces can be satisfied. Furthermore, since the variation of the cable force is continuous, the cable force, which is minimum at the last period can be preset as T_{pre} during the Newton–Euler equations' solution, which can improve the efficiency of the iteration. After calculation, if the cable force, which is minimum at the last period is not minimum this time, the minimum cable force at this time should be set as T_{pre} and then the solution that meets the requirements can be figured out by again solving the Newton–Euler equations.

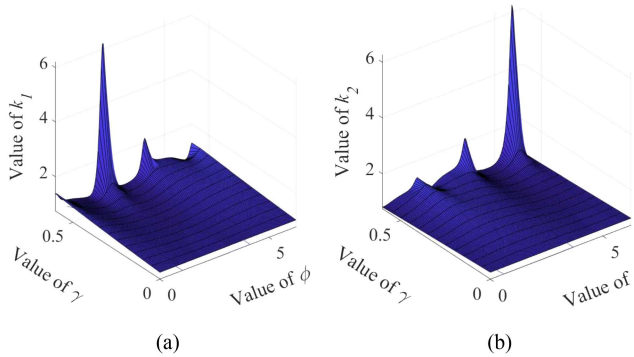

Fig. 7. Relation among k_1, k_2, φ, and γ. (a) Relation among φ, γ, and k_1. (b) Relation among φ, γ, and k_2.

It has been verified that when the manipulator is in the reachable space, the coefficient matrix of (72) is nonsingular. Therefore, (72) must have a unique solution, i.e., theoretically proving that the moment equilibrium of Link_i and HR_i can be achieved by setting the driving forces. In fact, if the values of $T_{i,i,3}, T_{i,i+6,3}, T_{i,i+12,3}$ can be positive and negative, the moment equilibrium of Link_i and HR_i could be achieved by 2 driving forces, and the 2 driving forces are unique. However, the driving force is the cable's tension force, i.e., the value is always positive, so 3 driving forces should drive the joint together to drive the Link_i successfully and scheme the driving forces uniformly.

It is also worth noting that if γ closes to the joint limit, the values of k_1 and k_2 would increase significantly or close to 0, which would lead to too large value difference among the driving forces and the balance would be hard to maintain.

2) Newton–Euler Equations: After one of the 3 driving forces on Link_i is set as T_{pre}, the ith Newton–Euler equations have 12 linear equations and 12 unknown variables. Equation (72) shows a way how to solve the Euler equations and Newton equations separately, which would reduce the calculation cost. Let $\boldsymbol{F_{1,2}} = 2F_{Ni,2x}\boldsymbol{v_{ix}} + 2F_{Ni,2y}\boldsymbol{v_{iy}} + F_{Ni,zc}\boldsymbol{v_{iz}}$, $\overline{\boldsymbol{F_{1,2}}} = x_{i,1}\,\boldsymbol{v_{ix}} + x_{i,2}\boldsymbol{v_{iy}}$, $\boldsymbol{F_{3,4}} = 2F_{Ni,4x}\boldsymbol{v_{ix}} + 2F_{Ni,4z}\boldsymbol{v_{iz}} + F_{Ni,yc}\boldsymbol{v_{iy}}$, $\overline{\boldsymbol{F_{3,4}}} = x_{i,3}\ \ \boldsymbol{v_{ix}} - x_{i,4}\boldsymbol{v_{iz}}$, then $\boldsymbol{F_{1,2}} + \overline{\boldsymbol{F_{1,2}}} = \boldsymbol{F_{Ni,1}} + \boldsymbol{F_{Ni,2}}$, $\boldsymbol{F_{3,4}} + \overline{\boldsymbol{F_{3,4}}} = \boldsymbol{F_{Ni,3}} + \boldsymbol{F_{Ni,4}}$. Let $\boldsymbol{F'_{3,4}} = \boldsymbol{F_{N(i+1),3}} + \boldsymbol{F_{N(i+1),4}}$, then Newton equations are as follows:

$$\begin{cases} -\boldsymbol{F_{1,2}} = \overline{\boldsymbol{F_{1,2}}} + \boldsymbol{F'_{3,4}} - \boldsymbol{S_{T1}} - \boldsymbol{S_{T2}} - \boldsymbol{G_i} - \boldsymbol{F_{I,i}} \\ \boldsymbol{F_{1,2}} + \boldsymbol{F_{3,4}} = -\overline{\boldsymbol{F_{1,2}}} - \overline{\boldsymbol{F_{3,4}}} - \boldsymbol{F_{IH,i}} - \boldsymbol{G_H} \end{cases}. \tag{77}$$

Then, all related forces including the driving forces on Link_i and HR_i can be solved by (72) and (77) with much less calculation. And then all related forces of the manipulator can be solved through the inward iteration. Afterward, the driving torques of all motors can be solved. Finally, the inverse dynamics is completed.

TABLE I
PARAMETERS OF THE CSM

Item	Value	Unit
Manipulator size (Without base box)	Ø120 × 2009	mm
Arm span	2.09	m
Total mass	10.5	kg
Degree of freedom	13	DOF
Num of motors	19	/
Cantilever load capability	5	kg
Accuracy	2	mm

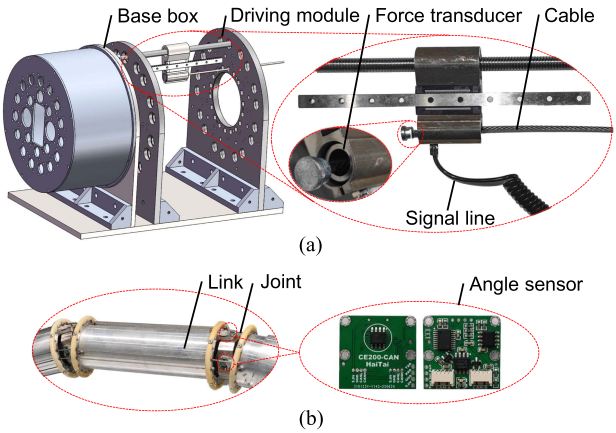

Fig. 8. Sensors' configuration. (a) Way of how the cable force transducer is assembled. (b) Way of how the joint angle sensors are assembled.

IV. EXPERIMENT

The experiments have been presented on a CSM physical prototype to verify the effectiveness of the kinematic and dynamic models. There are two types of experiments. The first is about the static tests, which study the cable forces when the manipulator stays in the homing position. The second experiment is about the dynamic tests, which study the cable forces when the manipulator stays in motion. Parameters of the CSM have been listed in Table I.

There are two special sensors on the manipulator. First, a force transducer is set on the driving module's end for each cable, which is for the cable force's monitoring. Second, two joint angle sensors are set on each joint, which are for monitoring the joint parameters and then deriving the end-effector pose. Fig. 8 shows how the cable force transducers and the joint angle sensors are assembled.

A. Static Experiment

Experiment purpose: Verify the accuracy of the driving force predicted by the models, when the CSM is static.

Experiment procedures:

1) Loosen all cables and let the manipulator naturally lie on the sliding table.
2) Tension all cables and let the manipulator in an uncertain posture.
3) Drive the motors, and let the manipulator return to and remain in the homing position from the uncertain posture. Keep the error of each universal joint angle less than 0.01°.
4) Read the feedback value of each force transducer every second. Read a total of 100 times and average the feedback values. The average data are recorded as $\emptyset_A$.
5) Repeat the above steps for 15 times.

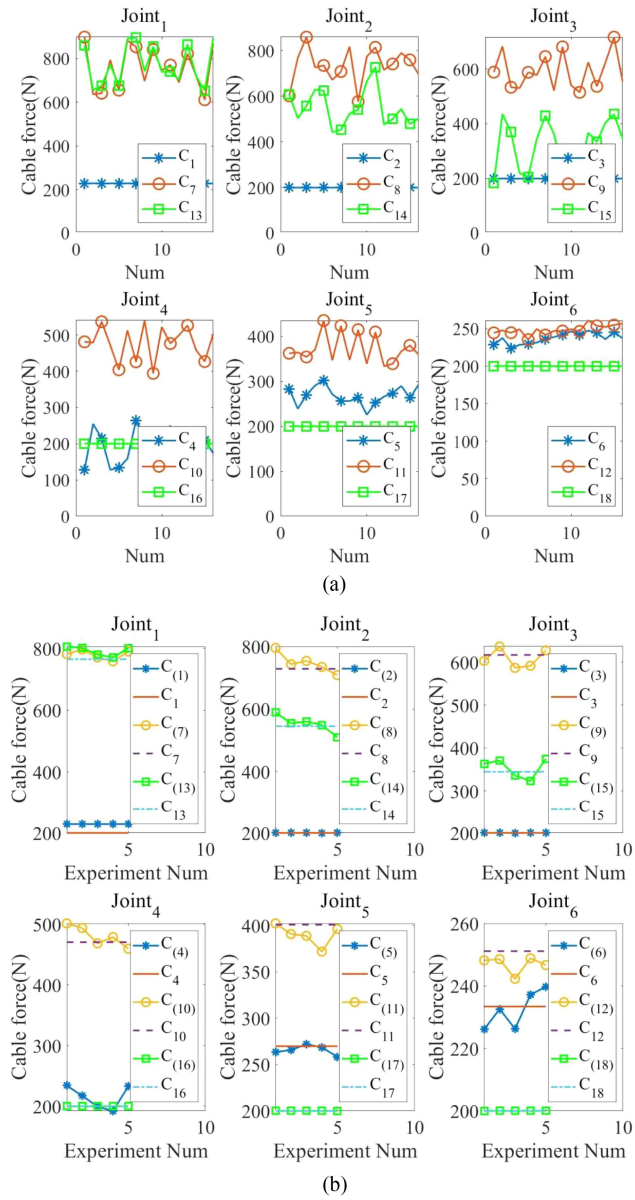

Fig. 9. Cable forces' recordings in static state. (a) Cable forces' recording in one experiment. (b) Cable forces' recording with the new averaged data.

Fig. 9(a) shows all feedback cable forces in one experiment. Every single figure shows 3 driving forces that drive the same joint. Every single cable force in the figures fluctuates with errors. There are 2 main reasons for that. One is the random errors

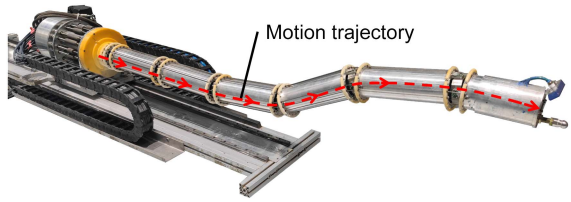

Fig. 10. Manipulator's motion in dynamic state.

caused by complex coupling effects among the cable forces. For instance, when the manipulator remains in the homing position, if the cable forces of C_6, C_{12}, C_{18} increase, the cable forces of C_5, C_{11}, C_{17} would decrease. The other is the systematic errors caused by the force transducers, such as zero-drift and linearity errors. Furthermore, the inadequate accuracy of the mass and geometric dimension would also lead to some small errors.

The above experiment has been repeated to reduce the random errors. The 15 groups' data ($\emptyset_A$) of each experiment are averaged again, which are recorded as $\emptyset_B$. As is shown in Fig. 9(b), the slightly fluctuating polylines refer to the new averaged data $\emptyset_B$, and the straight lines refer to the theoretically calculated cable forces. It can be found that the fluctuations of the cable forces have been significantly reduced and the errors are within a reasonable range.

Experiment results: The static test results show that the measured cable forces fluctuate each time, indicating that the dynamic system of the manipulator is complex and the coupling effect among the cables cannot be ignored. However, if multiple groups of the data are averaged, the random errors would be sharply reduced and the theoretical driving forces are basically the same as the feedback values. That verifies the accuracy and reliability of the proposed models when dealing with the static problems of the manipulator.

B. Dynamic Experiment

Experiment purpose: Verify the accuracy of the driving force predicted by the models, when the CSM is dynamic.

Experiment procedures:

1) Let the manipulator in the homing position state.
2) Set the driving torques of the motors the same as the calculation result of the dynamic method, when the manipulator does the tip-following motion. Fig. 10 illustrates how the manipulator moves.
3) Read the feedback value of each force transducer every 0.1 seconds and record the data.

Fig. 11 shows the variation of the cable forces, and$C_1, C_2, \cdots C_{18}$ refer to the theoretical values, while $C_{(1)}, C_{(2)}, \cdots C_{(18)}$ refer to the feedback values. Fig. 12(a) is the variation of joint parameters, and $\alpha_4, \alpha_5, \alpha_6$ refer to the theoretical values, while $\alpha_{(4)}, \alpha_{(5)}, \alpha_{(6)}$ refer to the feedback values. It shows that when the joint angle is relatively large, insufficient rotation may occur. That is because the shortest cable on the joint would bend more severely, which results in a bending resistance effect. Fig. 12(b) shows the errors of the manipulator's end, including three-axis errors. The experiment

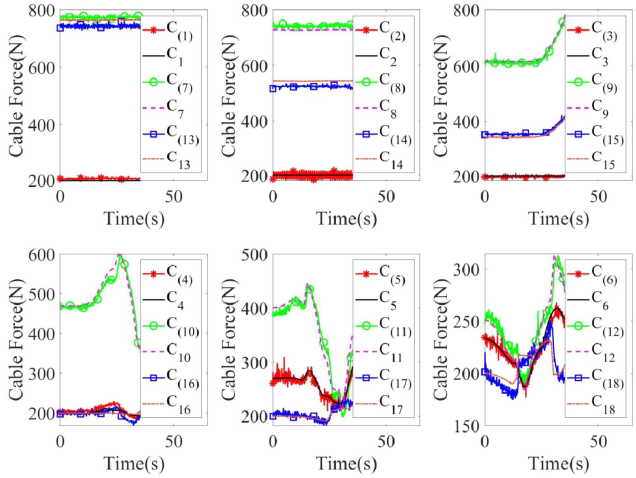

Fig. 11. Cable forces' recordings in dynamic state.

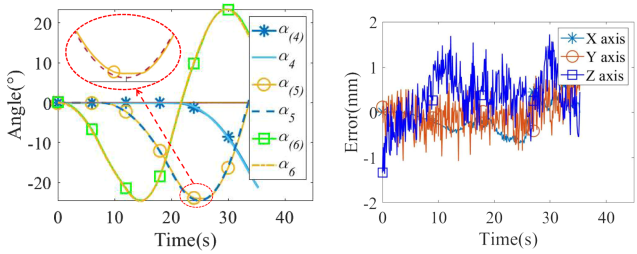

Fig. 12. Errors' analysis. (a) Variation of joint angles. (b) Variation of end effector errors.

proves that the theoretical driving forces are basically consistent with the real values during the motion, and simultaneously the dynamic accuracy is good.

Experiment results: The experiment data show that the coupling effect of the cable forces seems to be weakened in the dynamic tests, and the cable forces and the joint angles both are close to the theoretical values. Additionally, the algorithm of the kinematic and dynamic models works efficiently and reliably, which means it is applicable to real-time control. Therefore, the proposed method is practical.

C. Comparison Experiment

The comparison experiment with the conventional methods has been conducted to verify the advantages of the proposed method. Compared to traditional Newton–Euler methods [23], [24], [25], the paper constructs more direct and intuitive models skipping the intermediate joint parameters. Thus, according to the experiment, the computation efficiency of the kinematic parameters is improved by 23.9%. The result of the comparison experiment is shown in Table II.

In addition, since the traditional methods omit the analysis of hollow ring force, the modeling error is inevitable. "Theoretical driving force error" in Table II refers to the relative driving force difference between the traditional method and this article's method. Despite the tiny experiment difference, it

TABLE II
RESULT OF COMPARISON EXPERIMENT

Item	1)	2)
Computational complexity	$O(N)$	$O(N)$
Expression of pose information	Joint space & configuration space	Link Eigen vectors
Reference frame	With local frame	In global frame
Driving force optimization method	Solving the optimal objective function	Presetting strategy of driving forces
Average computing time/per step	0.21 ms	0.17 ms
Theoretical driving force error	1.9%	/

1) Conventional Newton–Euler method. 2) New Newton–Euler method in this article.

would increase with the increasing speed of CSM. And although CSM's motion is still slow at present, it will be faster with the development of technology. And when CSM's end acceleration is more than $10\mathrm{m}/\mathrm{s}^2$ in some cases, the theoretical driving force error could be more than 10%.

Moreover, to confirm the reliability and efficiency of the method, we have tested various trajectories on the CSM.

V. CONCLUSION

While the sufficient DOFs of hyper-redundant manipulator bring extremely flexible motion performance, it also challenges the more complex kinematic and dynamic algorithms. The excellent motion control should be not only efficient and stable, but also draw out the super dexterity of the hyper-redundant manipulator. Based on the widely used tracking geometric curve method, the paper reconstructs the kinematic and dynamic models in the global coordinate system with the link eigenvectors. And based on the new models, the manipulator's mechanics and the Newton–Euler equations are optimized and simplified. Thus, the dynamic solution can be obtained precisely and quickly with a reliable solving process. The experiments prove that the cable driving forces are optimized and the motion accuracy and smoothness are also improved. And the comparison with the traditional methods shows the improvements in efficiency and accuracy.

However, as the research went by, we also found a series of issues that have not been resolved but are worthy of further study. When the universal joint angle is close to the limit, the relations among the driving forces may change significantly, and some cables may even have severe bending effect. That would affect the driving of the joint. Later, we will study the ways of how to weaken these effects, such as setting T_{pre} dynamically, optimizing the mechanical structure. In addition, the complex coupling effects of the cables would cause random errors. Next, we will research and try to grasp the coupling laws. And that could not only furtherly verify the correctness of the dynamic model, but also is conducive to achieving the more precise dynamic close-loop control. Furtherly, we will also study the forward dynamics of the CSM according to the proposed method, so as to facilitate the dynamics optimization and the simulation of the manipulator.

REFERENCES

[1] K. Xu, J. Zhao, and M. Fu, "Development of the SJTU unfoldable robotic system (SURS) for single port laparoscopy," *IEEE/ASME Trans. Mechatron.*, vol. 20, no. 5, pp. 2133–2145, Oct. 2015.

[2] J. Kim, S.-I. Kwon, Y. Moon, and K. Kim, "Cable-movable rolling joint to expand workspace under high external load in a hyper-redundant manipulator," *IEEE/ASME Trans. Mechatron.*, vol. 27, no. 1, pp. 501–512, Feb. 2022.

[3] M. M. Tonapi, I. S. Godage, and I. D. Walker, "Next generation rope-like robot for in-space inspection," in *Proc. IEEE Aerosp. Conf.*, 2014, pp. 1–13.

[4] R. Buckingham and A. Graham, "Nuclear snake-arm robots," *Ind. Robot.*, vol. 39, no. 1, pp. 6–11, 2012.

[5] H. Tsukagoshi, A. Kitagawa, and M. Segawa, "Active hose: An artificial elephant's nose with maneuverability for rescue operation," in *Proc. IEEE Int. Conf. Robot. Autom.*, 2001, vol. 3, pp. 2454–2459.

[6] G. S. Chirikjian and J. W. Burdick, "An obstacle avoidance algorithm for hyper-redundant manipulators," in *Proc. IEEE Int. Conf. Robot. Autom.*, 1990, vol. 1, pp. 625–631.

[7] Z. Zhang, G. Yang, and S. H. Yeo, "Inverse kinematics of modular cable-driven snake-like robots with flexible backbones," in *Proc. IEEE 5th Int. Conf. Robot., Autom. Mechatron.*, 2011, pp. 41–46.

[8] I. D. Walker and M. W. Hannan, "A novel 'elephant's trunk' robot," in *Proc. IEEE/ASME Int. Conf. Adv. Intell. Mechatron.*, 1999, pp. 410–415.

[9] M. W. Hannan and I. D. Walker, "The 'elephant trunk' manipulator, design and implementation," in *Proc. IEEE/ASME Int. Conf. Adv. Intell. Mechatron.*, 2001, vol. 1, pp. 14–19.

[10] M. W. Hannan and I. D. Walker, "Kinematics and the implementation of an elephant's trunk manipulator and other continuum style robots," *J. Robot. Syst.*, vol. 20, no. 2, pp. 45–63, Feb. 2003, doi: 10.1002/rob.10070.

[11] F. Naccarato and P. C. Hughes, "Inverse kinematics of variable-geometry truss manipulators," *J. Robotic Syst.*, vol. 8, no. 2, pp. 249–266, Apr. 1991.

[12] G. S. Chirikjian and J. W. Burdick, "A modal approach to hyper-redundant manipulator kinematics," *IEEE Trans. Robot. Autom.*, vol. 10, no. 3, pp. 343–354, Jun. 1994.

[13] H. Xie, C. Wang, S. Li, L. Hu, and H. Yang, "A geometric approach for follow-the-leader motion of serpentine manipulator," *Int. J. Adv. Robot. Syst.*, vol. 16, no. 5, pp. 1–18, Sep. 2019, doi: 10.1177/1729881419874638.

[14] A. Aristidou and J. Lasenby, "FABRIK: A fast, iterative solver for the inverse kinematics problem," *J. Robot. Syst.*, vol. 73, pp. 243–260, 2011.

[15] Z. Mu, H. Yuan, W. Xu, T. Liu, and B. Liang, "A segmented geometry method for kinematics and configuration planning of spatial hyper-redundant manipulators," *IEEE Trans. Syst. Man Cybern. Syst.*, vol. 50, no. 5, pp. 1746–1756, May 2020.

[16] R. J. Williams and A. Seireg, "Interactive modeling and analysis of open or closed loop dynamic systems with redundant actuators," *J. Mech. Des.*, vol. 101, no. 3, pp. 407–416, Jan. 1979.

[17] D. E. Orin, R. B. McGhee, M. Vukobratovic, and G. Hartoch, "Kinematic and kinetic analysis of open-chain linkages utilizing Newton-Euler methods," *Math. Biosci.*, vol. 43, no. 1–2, pp. 107–130, Feb. 1979.

[18] M. Vukobratovic, "Computer method for dynamic model construction of active articulated mechanisms using kinetostatic approach," *Mech. Mach. Theory*, vol. 13, no. 1, pp. 19–39, 1978.

[19] G. Rodriguez, "Kalman filtering, smoothing, and recursive robot arm forward and inverse dynamics," *IEEE J. Robot. Autom.*, vol. 3, no. 6, pp. 624–639, Dec. 1987.

[20] V. Falkenhahn, T. Mahl, A. Hildebrandt, R. Neumann, and O. Sawodny, "Dynamic modeling of bellows-actuated continuum robots using the Euler–Lagrange formalism," *IEEE Trans. Robot.*, vol. 31, no. 6, pp. 1483–1496, Dec. 2015.

[21] D. C. Rucker and R. J. Webster III, "Statics and dynamics of continuum robots with general tendon routing and external loading," *IEEE Trans. Robot.*, vol. 27, no. 6, pp. 1033–1044, Dec. 2011.

[22] F. Campisano et al., "Closed-loop control of soft continuum manipulators under tip follower actuation," *Int. J. Robot. Res.*, vol. 40, no. 6–7, pp. 923–938, Jun. 2021.

[23] T. Wang, Z. You, W. Song, and S. Zhu, "Dynamic analysis of an underwater cable-driven manipulator with a fluid-power buoyancy regulation system," *Micromachines*, vol. 11, no. 12, pp. 1–14, Dec. 2020.

[24] W. Xu, T. Liu, and Y. Li, "Kinematics, dynamics, and control of a cable-driven hyper-redundant manipulator," *IEEE/ASME Trans. Mechatron.*, vol. 23, no. 4, pp. 1693–1704, Aug. 2018.

[25] W. Li, X. Huang, L. Yan, H. Cheng, B. Liang, and W. Xu, "Force sensing and compliance control for a cable-driven redundant manipulator," *IEEE/ASME Trans. Mechatron.*, pp. 1–12, Apr. 2023, doi: 10.1109/TMECH.2023.3263922.
[26] Z. Liu, X. Zhang, Z. Cai, H. Peng, and Z. Wu, "Real-time dynamics of cable-driven continuum robots considering the cable constraint and friction effect," *IEEE Robot. Autom. Lett.*, vol. 6, no. 4, pp. 6235–6242, Oct. 2021.
[27] W. S. Rone and P. Ben-Tzvi, "Continuum robot dynamics utilizing the principle of virtual power," *IEEE Trans. Robot.*, vol. 30, no. 1, pp. 275–287, Feb. 2014.
[28] A. Amouri, C. Mahfoudi, and A. Zaatri, "Dynamic modeling of a spatial cable-driven continuum robot using Euler–Lagrange method," *Int. J. Eng. Technol. Innov.*, vol. 10, no. 1, pp. 60–74, Jan. 2020.
[29] H. Yuan, L. Zhou, and W. Xu, "A comprehensive static model of cable-driven multi-section continuum robots considering friction effect," *Mech. Mach. Theory*, vol. 135, pp. 130–149, May 2019.

Xiantong Xu received the B.S. degree in mechanical engineering and automation from the Zhejiang University of Technology, Hangzhou, China, in 2009. He is currently working toward the Ph.D. degree in mechatronic engineering with Zhejiang University, Hangzhou.

His current research interests include kinematics, dynamics, and motion control of redundant manipulators.

Haibo Xie received the Ph.D degree in mechatronic engineering from the Zhejiang University, Hangzhou, China, in 2004.

He works as a professor with the State Key Laboratory of Fluid Power and Mechatronic Systems, Zhejiang University. His current research interests include redundant robotics, mobile hydraulic control systems and components, and tunneling boring machine driving technique.

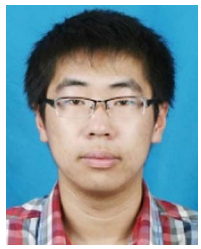

Cheng Wang received the B.S. degree in mechatronic engineering from the China University of Mining and Technology, Beijing, China, in 2014. He is currently working toward the Ph.D. degree in mechatronic engineering with Zhejiang University, Hangzhou, China.

His current research interests include cable-driven mechanisms, redundant manipulators, mechanics-based modeling, and control.

Huayong Yang received the Ph.D. degree in fluid power transmission and control from the University of Bath, Bath, U.K., in 1988.

He serves as an Academician with the China Engineering Academy. His current research interests include motion control and energy saving of mechatronic systems, microfluidic devices and systems, and R&D of fluid power components.